Supporting Information

Quantifying Nonradiative Recombination and Resistive Losses in Perovskite Photovoltaics: A Modified Diode Model Approach

Minshen Lin[1], Xuehui Xu[2], Hong Tian[2], Yang (Michael) Yang[2], Wei E. I. Sha[3]*, and Wenxing Zhong[1]**

[1]College of Electrical Engineering, Zhejiang University, Hangzhou 310027, China.

[2]State Key Laboratory of Modern Optical Instrumentation, Institute for Advanced Photonics, College of Optical Science and Engineering, Zhejiang University, Hangzhou 310027, China

[3]State Key Laboratory of Modern Optical Instrumentation, College of Information Science and Electronic Engineering, Zhejiang University, Hangzhou 310027, China

*Authors to whom correspondence should be addressed: yangyang15@zju.edu.cn, weisha@zju.edu.cn, and wxzhong@zju.edu.cn

Note 1. Defect-assisted recombination current from Shockley-Read-Hall model

The Shockley-Read-Hall model[1] describes the defect-assisted recombination rate as

$$U_{SRH} \approx \frac{np - n_i^2}{\tau_p n + \tau_n p}, \tag{S1}$$

where τ_n and τ_p are the respective defect-assisted recombination lifetimes for electrons and holes, inversely proportional to the concentration of defect states. As discussed in Section II, with higher applied voltage, more carriers are electrically injected into the bulk of the device and charge neutrality can gradually establish. This process is also illustrated in Fig. S1, where a device with predominant bulk SRH recombination is analyzed in terms of energy level and carrier concentration distributions. Moreover, the quasi-Fermi level splitting (QFLS) is equal to $q(V + JR_s)$ in the MD model, and $np = n_i^2 \exp(\mathrm{QFLS}/k_B T)$. In this case ($n \approx p$), Eq. (S1) can be simplified to

$$U_{SRH} = \frac{np - n_i^2}{(\tau_p + \tau_n)\sqrt{np}} = \gamma_{bulk} n_i \left[\exp\left(\frac{V + JR_s}{2k_B T/q}\right) - 1\right], \tag{S2}$$

where $\gamma_{bulk} = 1/(\tau_p + \tau_n)$ is the bulk SRH recombination coefficient. Integrating over the length of the absorption layer, L, we have the bulk SRH recombination current density,

$$J_{bulk}^{SRH} = qU_{SRH}L = qL\gamma_{bulk}n_i\left[\exp\left(\frac{V+JR_s}{2k_BT/q}\right)-1\right]. \quad \text{(S3)}$$

Likewise, the interface SRH recombination at the transport layer/perovskite interface can be described by the SRH formulation as

$$U_{SRH}^{if} \approx \frac{n^-p^+ - n_i^-n_i^+}{n^-/S_p + p^+/S_n}, \quad \text{(S4)}$$

where the superscripts of $\pm$ denote quantities evaluated at either the transport layer or perovskite side of the interfaces, and S_n, S_p are electron and hole recombination velocities[2]. However, at the interfaces, there is no simple relation between electron and hole densities that can be captured for simplifying Eq. (S4); hence, we use Eq. (3) with two undetermined parameters to describe the interface recombination current via curve fitting.

Note 2. Drift diffusion simulations

To study the performance of the modified diode (MD) model, we use drift-diffusion (DD) simulation results as the benchmarks for comparison. We use the well-established DD simulator, SCAPS[3], to produce the simulation results without regard to mobile ions. Unless particularly specified, the devices in DD simulations have the parameter values listed in Table S1. Besides, in the DD simulations, the radiative recombination coefficient is determined in such a way that the volumetric radiative recombination current equals the areal radiative recombination current calculated by the principle of detailed balance. This setting fulfills the principle of detail balance and in the limiting case, the DD simulations can reproduce the detailed balance limits[4]. In the course of curve fitting, all the parameters in the MD model are allowed to vary within a broad range (from 0 to 10^{12}).

To investigate the impact of ions on the steady-state performance of perovskite photovoltaics, SolarDesign[2] and IonMonger[3] are used to simulate the JV curves with varying ionic vacancy densities. The device parameters used for simulation are mostly the same as the template device[3], except for the parameters associated with bulk and interface SRH recombination, which are given in Table S3.

The details of modeling methods are described as follows. The governing equations of the drift-diffusion model without regarding to mobile ions are:

$$\begin{cases} \nabla\cdot(\varepsilon_r\nabla\psi) = q(n-p), \\ \dfrac{\partial n}{\partial t} = \dfrac{1}{q}\nabla\cdot J_n + G - R, \\ \dfrac{\partial p}{\partial t} = -\dfrac{1}{q}\nabla\cdot J_p + G - R, \end{cases} \quad \text{(S10)}$$

where $J_n = -q\mu_n n\nabla\psi + qD_n\nabla n$ and $J_p = -q\mu_p p\nabla\psi - qD_p\nabla p$ are the electron and hole current densities, respectively. The electron (hole) diffusion coefficient satisfies the Einstein relation $D_{n(p)} = \mu_{n(p)}k_BT/q$ and $\mu_{n(p)}$ is the electron (hole) mobility. Furthermore, $G = G^{ph} + G^{dark}$ is the total generation rate, where G^{ph} is the photon generation and G^{dark} is the dark generation at thermal equilibrium. Similarly, $R = R^{rad} + R^{nonrad}$ is the recombination rate at non-equilibrium states where R^{rad} is the radiative recombination rate and R^{nonrad} is the non-radiative recombination rate.

In perovskite photovoltaics, the non-radiative recombination is mainly due to the following defect-assisted Shockley-Read-Hall (SRH) recombination. The bulk SRH recombination rate is given by

$$R_{SRH} = \frac{np}{\tau_n(p + p_t) + \tau_p(n + n_t)}, \tag{S11}$$

where τ_n and τ_p are the lifetimes of excess electrons and holes, respectively. The trap level E_t in the bandgap is used to compute the densities of electrons and holes with respect to the trap level, i.e., $n_t = N_C \exp[(E_t - E_C)/k_BT]$ and $p_t = N_V \exp[(E_V - E_t)/k_BT]$. Similarly, the SRH recombination fluxes R^E_{SRH} and R^H_{SRH} at the interfaces are given by[3]

$$R^{E,H}_{SRH} = \frac{n^- p^+}{\frac{1}{v_n^{E,H}}(p^+ + p_t^+) + \frac{1}{v_p^{E,H}}(n^- + n_t^-)}, \tag{S11}$$

where the superscripts $\pm$ denote quantifies evaluated at either the left- or right-hand side of the perovskite/transport layer interfaces, respectively.

To account for mobile ions in the perovskite layer, in Eq. (S10), Poisson's equation needs to be modified to include the immobile cation vacancies N_0 and halide ion vacancy density P; also, a continuous equation for ions needs to be added.

$$\begin{cases} \nabla\cdot(\varepsilon_r\nabla\psi) = q(n - p + N_0 - P), \\ \dfrac{\partial n}{\partial t} = \dfrac{1}{q}\nabla\cdot J_n + G - R, \\ \dfrac{\partial p}{\partial t} = -\dfrac{1}{q}\nabla\cdot J_p + G - R, \\ \dfrac{\partial P}{\partial t} = \nabla\cdot F^P, \end{cases} \tag{S12}$$

where $F^P = D_I\nabla P + \mu_I P\nabla\psi$ is the flux of ion vacancy density, and D_I and μ_I are the ionic diffusion coefficient and mobility, respectively.

Note 3. Loss analysis

To study the impact of each loss pathway on the power conversion efficiency (PCE) of photovoltaics, we introduce an approach to calculating the normalized PCE gains. As discussed in Section 2.2, the influences of each loss are coupled in such a way that reducing one loss can give rise to a decrease in the others. We choose the maximum power point (MPP) of the device, where the PCE is evaluated, as the point of interest for comparison. Based on the device involving all losses at hand, in the DD simulation or the MD model, we exclude each loss pathway one at a time and calculate the PCE gains with respect to each loss. In the DD simulation, we exclude the loss pathway by making the corresponding simulation parameter inactive, while in the MD model, we do this by deleting the corresponding term in Eq. (1): for example, we exclude R_s by setting the value of R_s to zero yet keeping others the same, or we just delete the term J_{SRH}^{bulk} to exclude the effect of bulk SRH recombination. In this way, we can evaluate the impact of each loss, and normalize them as the normalized PCE gain:

$$\text{Normalized PCE Gain} = \frac{\text{PCE Gain without Loss } i}{\sum_i \text{PCE Gain without Loss } i} \times 100\%. \tag{S5}$$

This indicator can be viewed as a quantity that describes the influence of a loss pathway in percentage, which demonstrates their relative importance in a complete device.

Note 4. Differential ideality factor in the presence of series resistance

Taking series resistance into account, the recombination current is given by

$$J_{rec} = J_o \exp\left[\frac{q(V + JR_s)}{n_{id} k_B T}\right]. \tag{S6}$$

Assuming that the ideality factor, n_{id}, and the series resistance, R_s, are independent of applied voltage (this is consistent with the parameter retrieval process of curve fitting that produces voltage-independent parameters), we can find an expression for n_{id} by differentiating the above equation with respect to V, i.e.,

$$\frac{dJ_{rec}}{dV} = J_{rec} \frac{q}{n_{id} k_B T} \left(1 + \frac{dJ}{dV} R_s\right). \tag{S7}$$

Reordering the terms, we have

$$n_{id} = \frac{q}{k_B T} \left(\frac{d \ln J_{rec}}{dV}\right)^{-1} \left(1 + \frac{dJ}{dV} R_s\right). \tag{S8}$$

In the exponential region of the JV curve, J_{rec} is the predominant current density loss such that $dJ/dV = -dJ_{rec}/dV$. Thus, we can substitute J_{rec} in place of J,

$$n_{id} = \frac{q}{k_B T} \left(\frac{d \ln J_{rec}}{dV}\right)^{-1} \left(1 - \frac{dJ_{rec}}{dV} R_s\right). \tag{S9}$$

Using Eq. (S9), the calculated n_{id} varies with voltage, and the retrieved value lies in the exponential region, close to the minimum differential ideality factor, as shown in Fig. 3.

Note 5. Device Fabrication and Characterization

The devices in this paper were made from commercially available products. C_{60}, FAI, PbI_2, CsI, n-Octylammonium Iodide (OAI), and BCP were purchased from Xi'an Polymer Light Technology Corporation. Dimethyl formamide (DMF), dimethyl sulfoxide (DMSO), acetone, and chlorobenzene (CB) isopropanol (IPA), were purchased from J&K Scientific. Meo-2PACz were purchased from TCI(Shanghai)Development Co., Ltd. ITO substrates (86% transmittance, 15 Ohm·sq^{-1}) were purchased from South China Xiangcheng Technology Co., Ltd.

The ITO glasses were sequentially cleaned in deionized water, acetone, and IPA by sonication for 5 min. Before deposition of the hole transporting layer, all ITO glasses were further cleaned for 20 min by a UV-ozone machine. To deposit the hole transporting layer, 0.4mg/ml Meo-2PACz iso-propyl alcohol solution was spin-coated onto ITO glasses at 5000 rpm for 30 s in the N_2 glove box and annealed at 100 ℃ for 10 min. The HTL thickness was measured to be 10 nm. The perovskite precursor solution was prepared by mixing 645.5 mg PbI_2, 228.7 mg FAI, 28.3 mg CsI, and 200 μL DMSO in 800 μL DMF solvent. All the solutions were stirred at 60 ℃ over 2 hours and filtered with a 0.22 μm polytetrafluoroethylene filter before use. The perovskite layer of Device 1 was prepared in ambient air with a humidity of 60%, while Device 2 was made in the N_2 glove box with standard procedure. The perovskite films with thicknesses of 750 nm were deposited by two-step spin-coating progress at first 1000 rpm for 10 s with a ramp of 1000 rpm·s^{-1}, and then 4000 rpm for 25 s with a ramp of 4000 rpm·s^{-1}. 200 μL chlorobenzene (CB) was dropped onto the film ~10 s before the end of the procedure and then annealed at 100 ℃ for 10 min under a different atmosphere. For the interface-passivated sample, 50ul of OAI (1mg/ml in IPA) was spun onto the perovskite layer with a speed of 5,000 rpm for 30 s without annealing. After that, 25nm C_{60}, 5nm BCP, and 100 nm Ag were coated onto the prepared sample by the thermal evaporation method sequentially.

The standard current density-voltage (JV) measurements and stabilized current at fixed voltage measurements were carried out by a Keithley 2400 source meter under AM 1.5G illumination from the xenon arc lamp of a Class A solar simulator. The light intensity was calibrated by a reference mono-crystalline Si solar cell. The JV measurements under laser irradiance were carried out by a Keithley 2460 source meter under the illumination of a 760 nm laser. The irradiance of the laser was measured by an integrating sphere photodiode power sensor (Thorlabs S142C). The ultraviolet-visible (UV-Vis) absorbance measurements were conducted with an Agilent Cary 7000 UV-Vis spectrometer. The thicknesses of the films were

measured by XF-WSBX-2200125 Step-Profiler. Time-resolved photoluminescence (TRPL) spectra were measured with a home-setup confocal fluorescence system at room temperature by a time-correlated single photon counting (TCSPC) module (PicoHarp 300), a scratch pad memory (SPAD) detector (IDQ, id100) with an instrument response function of ~100 ps, and a picosecond 532 nm laser.

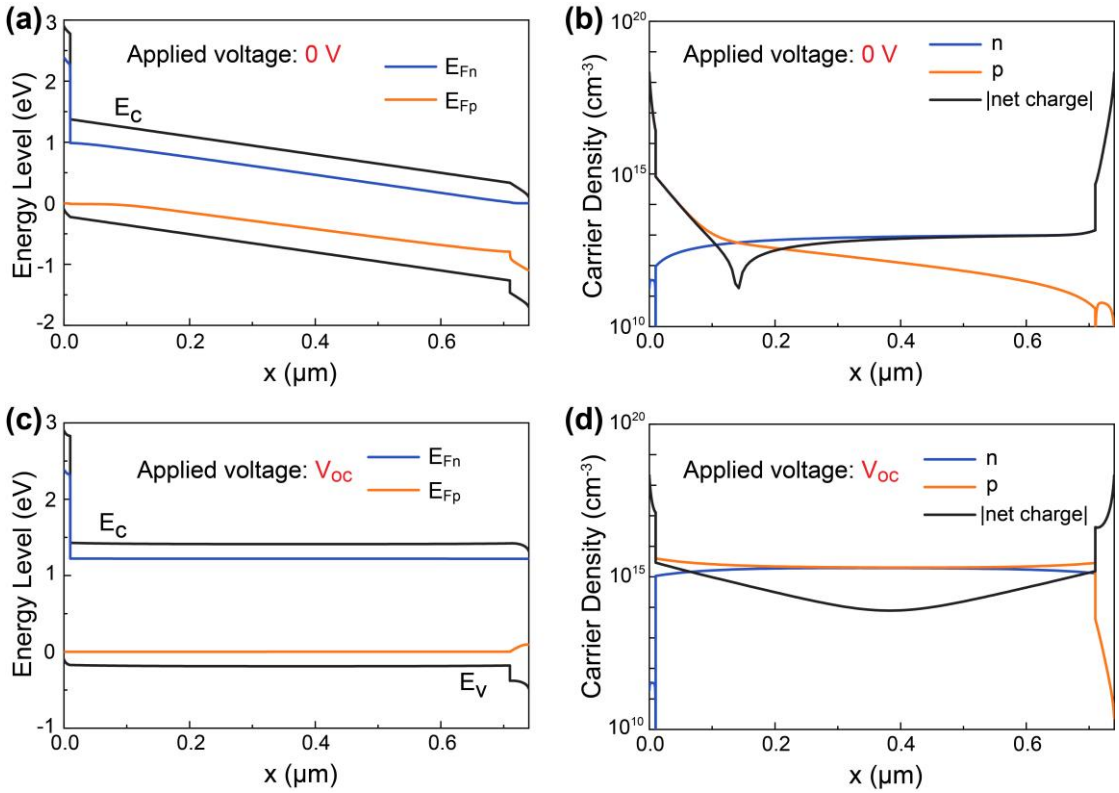

Figure S1. Energy level and carrier density distributions in the device with predominant bulk SRH recombination. **(a-b)** The distributions under an applied voltage of 0 V. **(c-d)** The distributions at open-circuit voltage. The irradiance is 1 Sun for all cases. It is noticeable in **(b)** and **(d)** that with higher applied voltage, more carriers are injected into the bulk of the device and charge neutrality establishes.

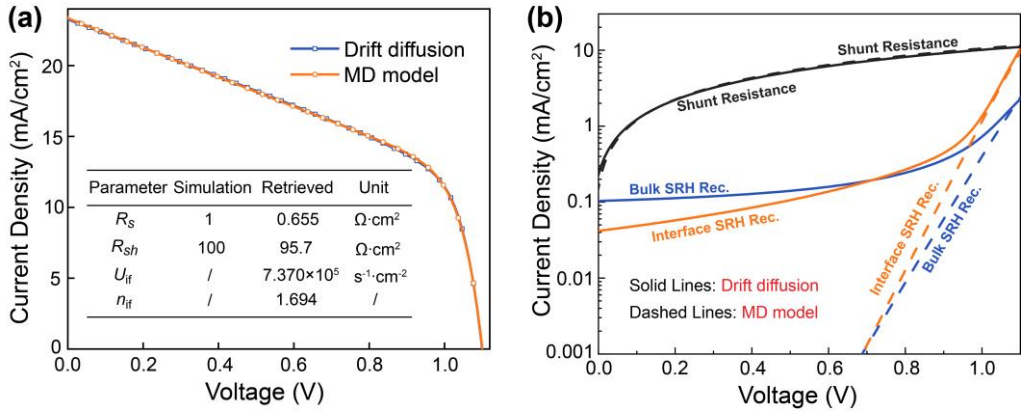

Figure S2. Current density-voltage relations of a device with severe shunt current leakage. The shunt current density calculated by MD model is consistent with the simulation result.

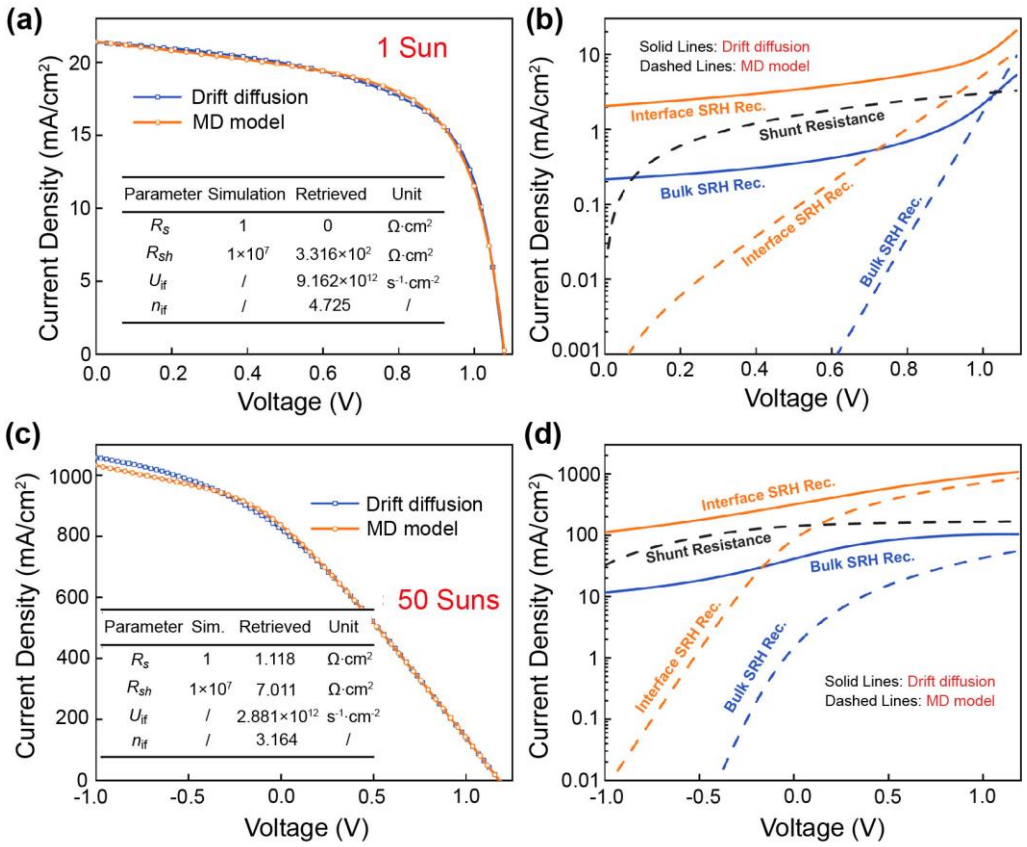

Figure S3. Current density-voltage relations of a device with severe interface SRH recombination. It is noticeable that the large recombination current in the low-voltage region bends the JV curve in a similar way as with R_{sh}. However, such increase in recombination current with respect to applied voltage cannot be perfectly described by R_{sh} with a fixed value, thereby introducing errors into the cost function.

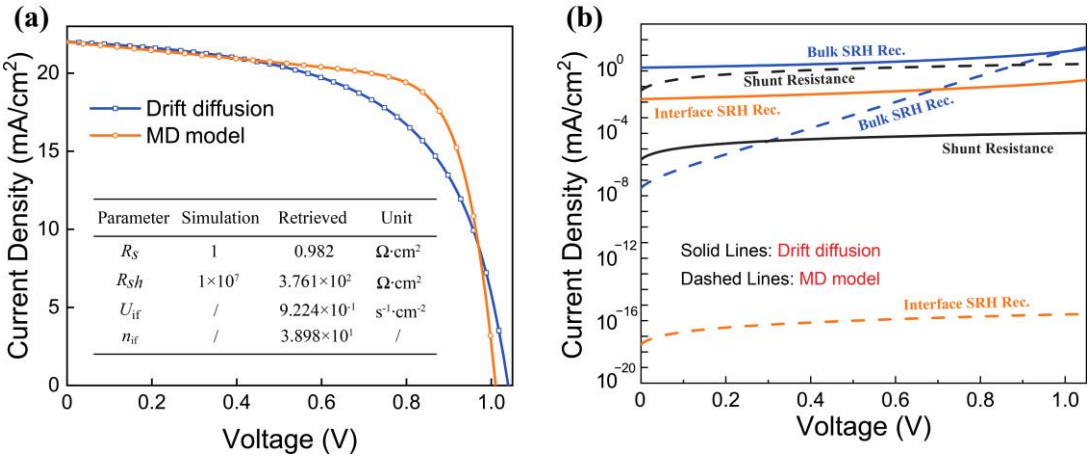

Figure S4. Current density-voltage relations of a device with severe bulk SRH recombination (10 ns recombination lifetime).

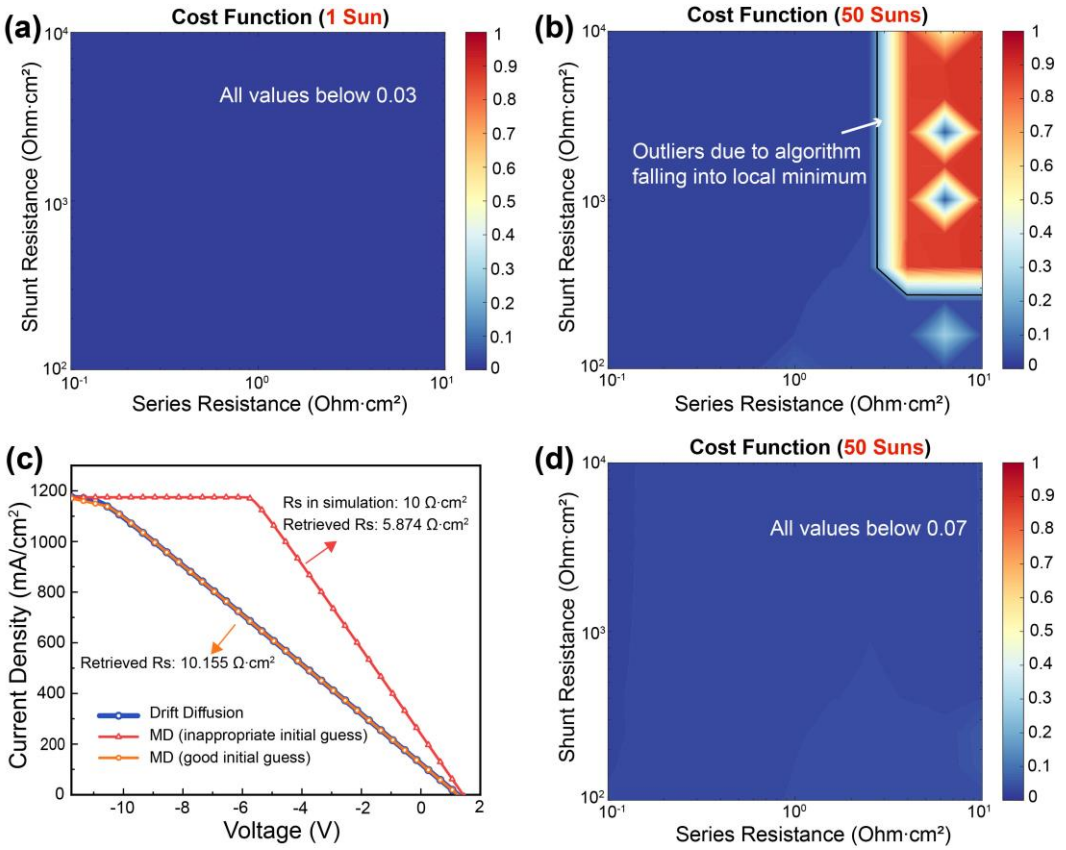

Figure S5. Contour plots of cost as a function of series resistance and shunt resistance. **(a-b)** is calculated by a fixed initial guess for R_s, 1 $\Omega \cdot \mathrm{cm}^2$, in the MD model. The outlier with a very high cost function is further analyzed in **(c)**, where we can see that a good initial guess for R_s is critical for the accuracy of curve fitting. With this knowledge, in **(d)**, we use the retrieved values of R_s in **(a)** as the initial guesses for fitting the 50 Suns curves, where uniformly low cost-function is achieved, showing that this strategy (or randomized initial guess) can help retrieve precise parameter values and validate model accuracy.

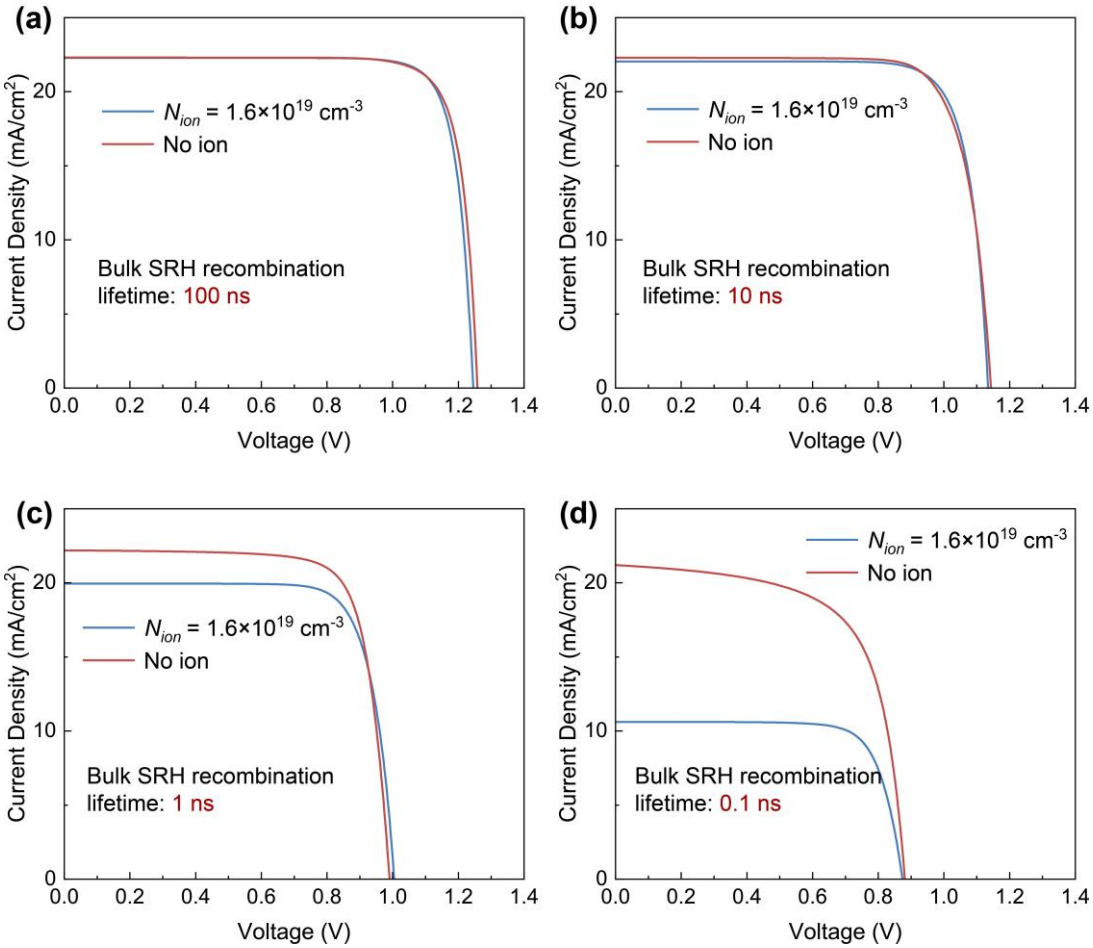

Figure S6. Simulated current density-voltage relations incorporating mobile ions for the device with predominant bulk SRH recombination. The bulk SRH recombination lifetimes are **(a)** 100 ns, **(b)** 10 ns, **(c)** 1 ns, and **(d)** 0.1 ns, respectively. The results are simulated with SolarDesign; identical trends can be reproduced by IonMonger.

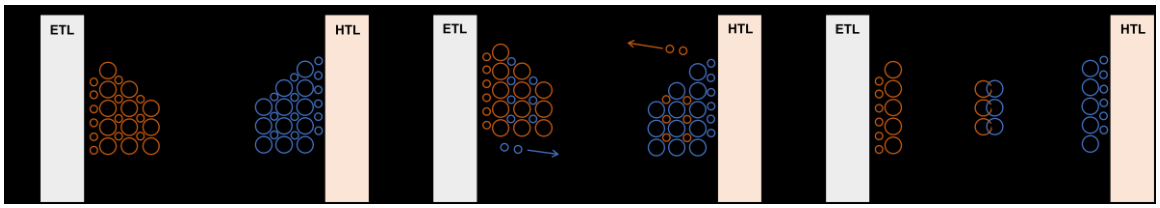

Figure S7. Ionic and electronic distributions and the corresponding band diagrams in perovskite photovoltaics: **(a)** in thermal equilibrium; **(b)** immediately upon illumination; **(c)** after sufficient time of illumination.

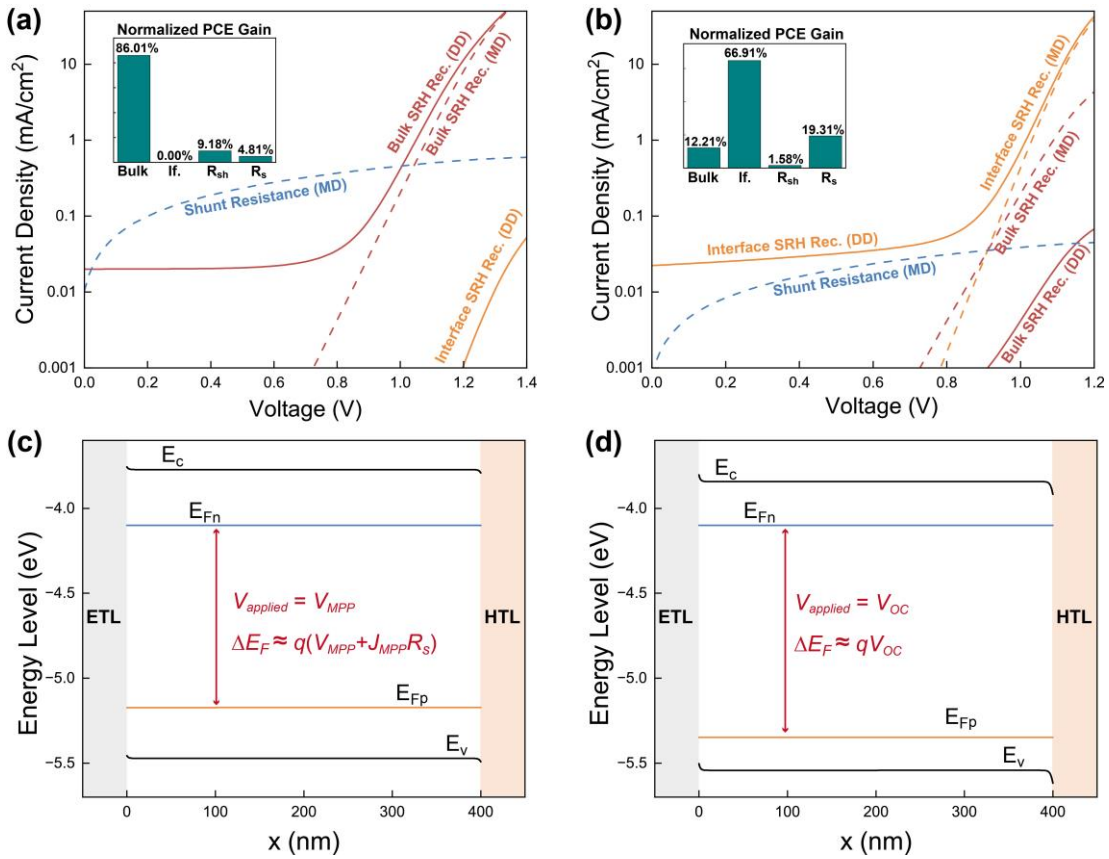

Figure S8. MD model fitting for steady-state *JV* curves incorporating 10^{25} m^{-3} ionic vacancies. **(a)** The predominant loss pathway is bulk SRH recombination. **(b)** The predominant loss pathway is interface SRH recombination. **(c)** Energy level diagram for bulk SRH recombination limited device at maximum-power-point voltage. **(d)** Energy level diagram for bulk SRH recombination limited device at open-circuit voltage.

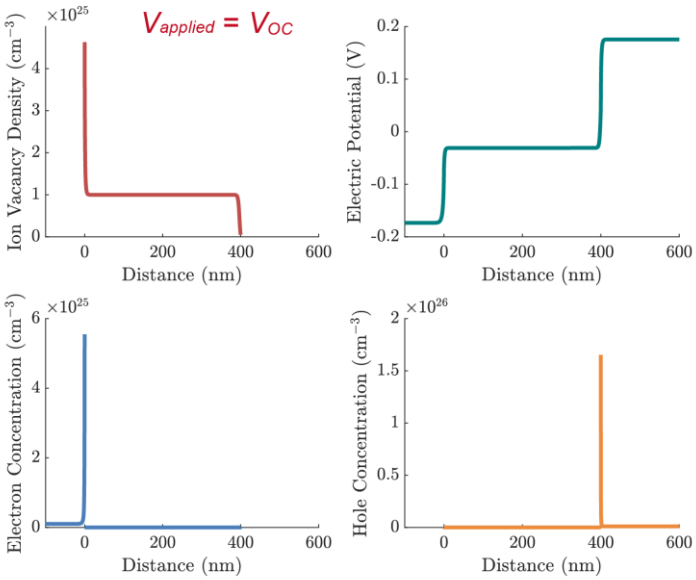

Figure S9. Ion vacancy density, carrier density, and electric potential distribution in the device with 10^{25} m^{-3} ionic vacancies at open-circuit voltage.

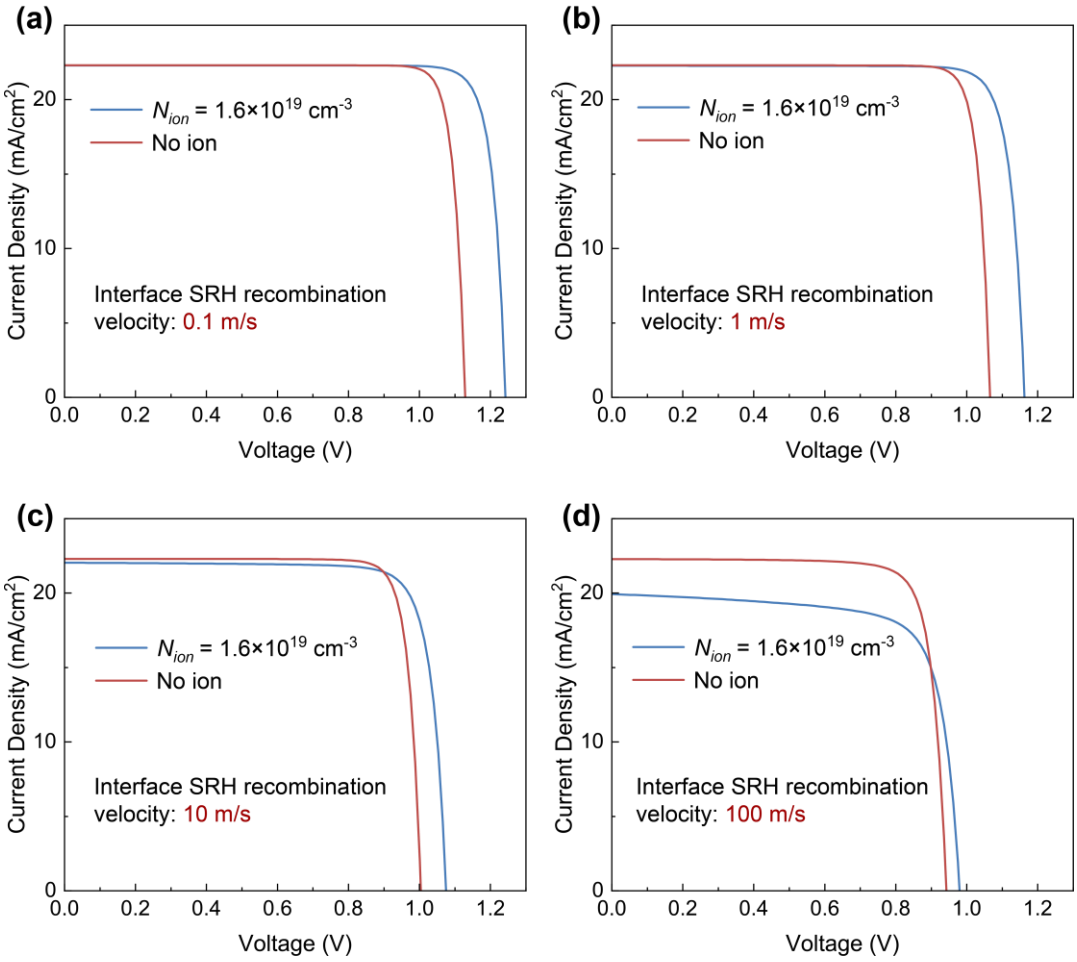

Figure S10. Simulated current density-voltage relations incorporating mobile ions for the device with predominant interface SRH recombination. The interface SRH recombination velocities are **(a)** 0.1 m/s, **(b)** 1 m/s, **(c)** 10 m/s, and **(d)** 100 m/s, respectively. The results are simulated with SolarDesign; identical trends can be reproduced by IonMonger.

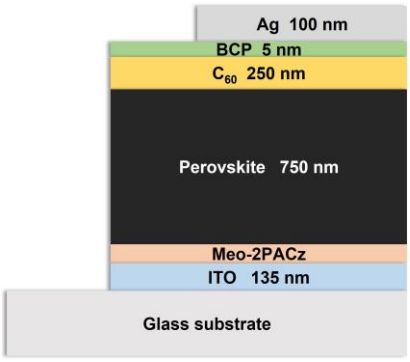

Figure S11. Device structure of the perovskite photovoltaics used in the experiments.

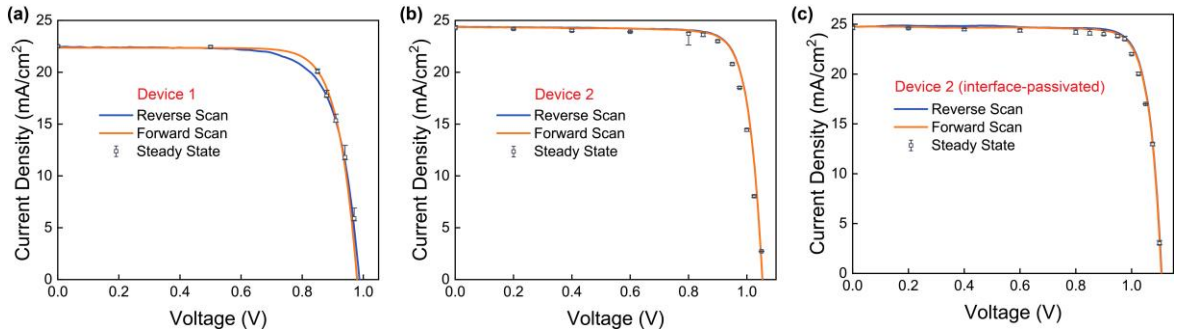

Figure S12. Current density-voltage relations of Device 1, Device 2, and interface-passivated Device 2. The range and average values of the recorded steady-state data points at specific voltages are also depicted in the corresponding figures.

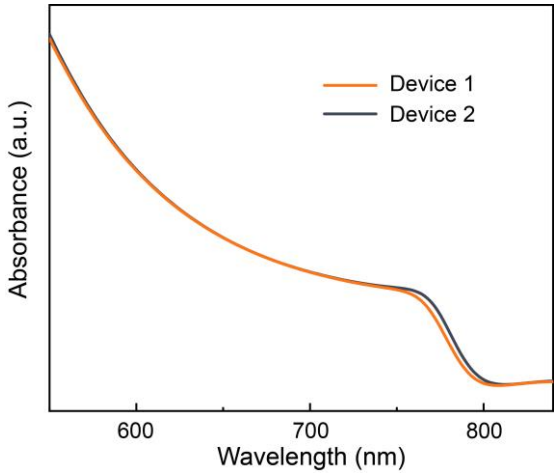

Figure S13. UV-vis absorbance as a function of wavelength.

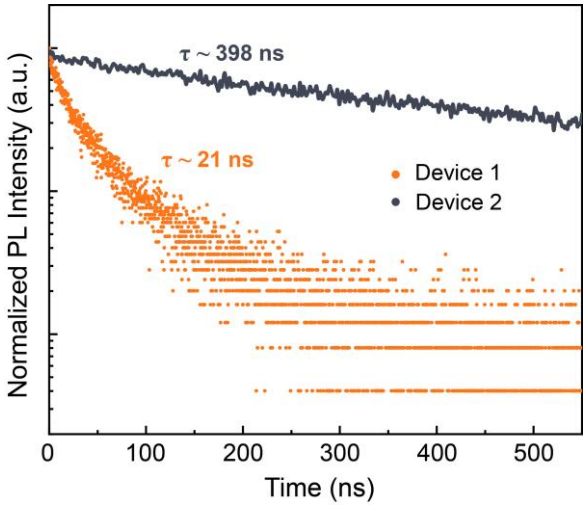

Figure S14. TRPL decay of the perovskite films. Device 1 and Device 2 denote that the film is made in the same condition as the corresponding device.

Table S1. Device parameters used for drift-diffusion simulations

Parameter	Symbol	Value	Unit
Thickness of PTAA	d_{PTAA}	10	nm
Thickness of perovskite	d_{pero}	700	nm
Thickness of C_{60}	d_{C60}	30	nm
Electron affinity of PTAA	$E_{A,\mathrm{PTAA}}$	2.5	eV
Bandgap of PTAA	$E_{G,\mathrm{PTAA}}$	3	eV
Electron affinity of perovskite	$E_{A,\mathrm{pero}}$	3.9	eV
Bandgap of perovskite	$E_{G,\mathrm{pero}}$	1.6	eV
Electron affinity of C_{60}	$E_{A,\mathrm{C60}}$	3.9	eV
Bandgap of C_{60}	$E_{G,\mathrm{C60}}$	1.8	eV
Work function of ITO	W_{ITO}	5.4	eV
Work function of Ag	W_{Ag}	4.0	eV
Relative dielectric constant of PTAA	ϵ_{PTAA}	3.5	/
Relative dielectric constant of perovskite	ϵ_{pero}	22	/
Relative dielectric constant of C_{60}	ϵ_{C60}	5	/
Effective density of states in PTAA	$N_{C/V,\mathrm{HTL}}$	1×10^{20}	cm^{-3}
Effective density of states in perovskite	$N_{C/V,\mathrm{pero}}$	3.1×10^{18}	cm^{-3}
Effective density of states in C_{60}	$N_{C/V,\mathrm{C60}}$	1×10^{20}	cm^{-3}
Carrier mobilities in PTAA	μ_{PTAA}	1.5×10^{-4}	$\mathrm{cm}^2/(\mathrm{Vs})$
Carrier mobilities in perovskite	μ_{pero}	1	$\mathrm{cm}^2/(\mathrm{Vs})$
Carrier mobilities in C_{60}	μ_{C60}	1×10^{-2}	$\mathrm{cm}^2/(\mathrm{Vs})$
Effective doping density in PTAA	N_A^-	0	cm^{-3}
Effective doping density in C_{60}	N_D^+	0	cm^{-3}
Electron lifetime for bulk SRH recombination*	τ_n	500	ns
Hole lifetime for bulk SRH recombination*	τ_p	500	ns
SRH recombination velocity at ETL/perovskite interface*	$S_{ETL/perov}$	2000	cm/s
SRH recombination velocity at HTL/perovskite interface*	$S_{HTL/perov}$	200	cm/s
Temperature	T	298	K
Radiative recombination coefficient	B_{rad}	9.8×10^{-12}	cm^4/s
Capture cross section	σ	1×10^{-15}	cm^2

Thermal velocity	v_{th}	1×10^7	cm/s
External series resistance*	R_s	1	$\Omega \cdot \mathrm{cm}^2$
External shunt resistance*	R_{sh}	1×10^7	$\Omega \cdot \mathrm{cm}^2$

Note: The parameter values are adopted from the references[6, 7], except the thickness of the perovskite layer and the parameters marked with asterisk symbols (indicating that they can be varied during the simulations).

Table S2. Retrieved MD model parameters for Device 2 under laser illumination

Irradiance ($\mathrm{W/cm^2}$)	Scan Direction	R_s ($\Omega \cdot \mathrm{cm}^2$)	R_{sh} ($\Omega \cdot \mathrm{cm}^2$)	U_{if} ($\mathrm{s^{-1}cm^{-2}}$)	n_{if}
0.1	F	0.416	1.343e3	1.719e8	1.930
	R	0.439	5.189e2	3.930e7	1.808
1.0	F	0.370	4.892e1	1.317e13	3.511
	R	0.383	8.607e1	4.805e12	3.239
2.0	F	0.380	3.164e1	2.053e13	3.450
	R	0.390	4.823e1	1.348e13	3.325
3.0	F	0.401	3.734e1	3.375e13	3.493
	R	0.392	3.907e1	2.072e13	3.325
4.0	F	0.363	5.189	1.607e13	3.170
	R	0.380	1.791e1	2.581e13	3.257
5.0	F	0.366	6.389	2.050e13	3.165
	R	0.384	9.737	1.506e13	3.053

Table S3. Device parameters used for drift-diffusion simulations incorporating ion migration

Predominant Recombination	Parameter	Value	Unit
Bulk SRH recombination	Electron pseudo-lifetime for SRH	100-0.1	ns
	Hole pseudo-lifetime for SRH	100-0.1	ns
	Electron recombination velocity for SRH	10^{-5}	m/s
	Hole recombination velocity for SRH	10^{-5}	m/s
Interface SRH recombination	Electron pseudo-lifetime for SRH	10^5	ns
	Hole pseudo-lifetime for SRH	10^5	ns
	Electron recombination velocity for SRH	0.1-100	m/s
	Hole recombination velocity for SRH	0.1-100	m/s

Table S4. Optimization strategies for different loss pathways

Predominant Loss Pathway	Optimization Strategies
Bulk SRH recombination	- Compositional engineering - Dimensionality engineering - Morphology optimization - Crystallization control
Interface SRH recombination	- Interface defect passivation - Band-level alignment - Morphology Control
Series resistance	- Metal grid - Transport layer doping - High mobility transparent conduction layers
Shunt resistance	- Reducing manufacturing defects - Reducing low-voltage recombination currents

Table S5. Causes to large fitting error and corresponding solutions

Causes to large fitting error	Solutions
Low bulk SRH recombination lifetime	Referring to TRPL results
High interface SRH recombination velocity	Identifying contributions of shunt resistance
Algorithm falling into local minimum	Using random sets of initial parameters

Table S6. Comparison between the MD model and classical models for photovoltaics

Model	Strengths	Weaknesses	Applications
Drift-Diffusion Models	- Physical insight - Broad applicability - Steady-state and transient behavior	- Too many parameters - Questionable parameter uniqueness - Parameter sensitivity - Numerical complexity	- Study device physics - Study complex device structures - Predict performance
Classical Diode Models	- Rapid computation - Parameter extraction	- Over-simplified parameters - Limited physical interpretability	- Predict performance - Design PV modules and arrays
MD Model (this work)	- Accurate loss quantification - Clear parameter physical meanings	- Domain-specific - Fitting error can be large in certain cases	- Quantify losses in perovskite PVs - Predict performance

References

[1] Shockley, W. & Read Jr, W. Statistics of the recombinations of holes and electrons. *Physical review* **87**, 835 (1952).

[2] SolarDesign. A photovoltaic device simulation and design platform, freely available online at solardesign.cn.

[3] Courtier, N. E., Cave, J. M., Walker, A. B., Richardson, G. & Foster, J. M. IonMonger: a free and fast planar perovskite solar cell simulator with coupled ion vacancy and charge carrier dynamics. *Journal of Computational Electronics* **18**, 1435-1449, doi:10.1007/s10825-019-01396-2 (2019).

[4] Burgelman, M., Nollet, P. & Degrave, S. Modelling polycrystalline semiconductor solar cells. *Thin Solid Films* **361-362**, 527-532, doi:https://doi.org/10.1016/S0040-6090(99)00825-1 (2000).

[5] Ren, X., Wang, Z., Sha, W. E. I. & Choy, W. C. H. Exploring the Way To Approach the Efficiency Limit of Perovskite Solar Cells by Drift-Diffusion Model. *ACS Photonics* **4**, 934-942, doi:10.1021/acsphotonics.6b01043 (2017).

[6] Stolterfoht, M. et al. (2018). Visualization and suppression of interfacial recombination for high-efficiency large-area pin perovskite solar cells. *Nature Energy*. DOI: 10.1038/s41560-018-0219-8.

[7] Caprioglio, P. et al. (2020). On the Origin of the Ideality Factor in Perovskite Solar Cells. *Advanced Energy Materials*. DOI: 10.1002/aenm.202000502.